



CO₂ methanation over Ni nanoparticles inversely loaded with CeO₂ and Cr₂O₃: Catalytic functions of metal oxide/Ni interfaces

Junbo Tian^{a,b,c,1}, Peng Zheng^{a,1}, Tengfei Zhang^c, Zhennan Han^{a,*}, Wenqing Xu^{c,*}, Fangna Gu^{c,d,**}, Fang Wang^e, Zhanguo Zhang^{a,f}, Ziyi Zhong^{b,g,***}, Fabing Su^{c,f,****}, Guangwen Xu^{a,f,*****}

^a Key Laboratory on Resources Chemicals and Materials of Ministry of Education, Shenyang University of Chemical Technology, Shenyang 110142, China

^b Guangdong Provincial Key Laboratory of Materials and Technologies for Energy Conversion (MATEC), GTIIT, Guangdong 515063, China

^c Institute of Process Engineering, Chinese Academy of Sciences, Beijing 100190, China

^d Beijing Key Laboratory of Enze Biomass Fine Chemicals, College of New Materials and Chemical Engineering, Beijing Institute of Petrochemical Technology, Beijing 102617, China

^e School of Ecology and Environment, Beijing Technology and Business University, Beijing 100048, China

^f Institute of Industrial Chemistry and Energy Technology, Shenyang University of Chemical Technology, Shenyang 110142, China

^g Department of Chemical Engineering, Guangdong Technion Israel Institute of Technology (GTIIT), 241 Daxue Road, Shantou 515063, China

ARTICLE INFO

Keywords:

CO₂ methanation
Ni catalyst
Reaction mechanism
Oxide-metal interface
Inverse loading

ABSTRACT

Interfaces between active metal and metal oxide in a heterogenous catalyst often play an important role in catalysis. In this work, we intentionally synthesized a series of inverse CeO₂-Cr₂O₃/Ni model catalysts with the formation of controlled CeO₂-Ni and Cr₂O₃-Ni interfacial structures and investigated the roles of the oxide-metal interfaces in CO₂ methanation performance through excluding the normal support effect. Experimental and DFT calculation results reveal that the formate pathway tends to occur on the catalyst with only CeO₂-Ni interfaces. The Cr₂O₃-Ni interface formed after introducing Cr oxide alters the nearby CeO₂-Ni interface by electron transfer through Ni, which brings an additional reaction pathway (CO pathway) on CeO₂-Cr₂O₃/Ni. Furthermore, it shows a relatively lower CO₂ absorption energy and activation energy barrier for CO₂ dissociation to CO at the Cr₂O₃-Ni interface, favorable for CO₂ activation and further hydrogenation, thus leading to excellent low-temperature activity.

1. Introduction

Metal/oxide (M/O) composites are the most widely used multi-component supported catalyst systems, in which M-O interfaces have been demonstrated to be an important factor in determining their catalytic performances [1,2]. Engineering and understanding the M-O interface are thus essential to guiding and designing catalysts for

excellent catalytic performance. In conventional M/O catalysts, oxides are often used as supports to stabilize the active metal nanoparticles, often generating strong metal-support interaction (SMSI) overlayers [3, 4] and new M-O interfaces [5]. Numerous reports have shown that SMSI could generate more specific M-O interfacial sites, facilitating certain fundamental reaction steps and ultimately leading to enhanced catalytic activity [6–8]. For example, Zhang et al. induced SMSI in a Ru/TiO₂

* Corresponding authors.

** Corresponding author at: Beijing Key Laboratory of Enze Biomass Fine Chemicals, College of New Materials and Chemical Engineering, Beijing Institute of Petrochemical Technology, Beijing 102617, China.

*** Corresponding author at: Guangdong Provincial Key Laboratory of Materials and Technologies for Energy Conversion (MATEC), GTIIT, Guangdong 515063, China.

**** Corresponding author at: Institute of Process Engineering, Chinese Academy of Sciences, Beijing 100190, China.

***** Corresponding author at: Key Laboratory on Resources Chemicals and Materials of Ministry of Education, Shenyang University of Chemical Technology, Shenyang 110142, China.

E-mail addresses: hanzhennan1989@163.com (Z. Han), wqxu@ipe.ac.cn (W. Xu), fangnagu@bpt.edu.cn (F. Gu), ziyi.zhong@gtiit.edu.cn (Z. Zhong), fbsu@ipe.ac.cn (F. Su), gwxxu@syuct.edu.cn (G. Xu).

¹ Junbo Tian and Peng Zheng contributed equally to this work.

catalyst by a reduction treatment to create the SMSI overlayer, thus increasing the number of Ru/TiO_x interfacial sites and promoting C–O bond cleavage with a higher TOF in the FTS reaction [6]. In addition, electron transfer between metal and oxide support also influences the chemical state of the metal sites, thus enhancing the corresponding catalytic activity [9–13]. However, in the conventional M/O catalyst, high temperatures are required to drive the oxide migration to the surface of supported active metal, creating uncontrollable overlayers, which may be difficult to distinguish the individual role of various O–M interfaces in the supported M/O catalysts.

The construction of an inverse O/M catalyst, which involves loading small inert oxide nanoparticles onto a large active metal substrate [14], enables the controlled modification of oxide species on the active metal surface. This approach highlights the crucial role played by the O–M interface while minimizing the impact of oxide supports. The preparation of inverse catalysts is not limited to specific techniques, such as atomic layer deposition and spray pyrolysis, but also includes traditional simple methods like impregnation and precipitation [15–17]. Furthermore, loading oxides onto the active metal surface to form inverse O/M catalysts may yield new electronic structures and catalytic properties, allowing for effective modeling of the strong metal-support interaction. In this case, the interfacial interactions are redefined as oxide-metal interactions (OMI) [1]. Inverse O/M catalysts have been employed in many reactions. G. M. Schwab originally proposed this kind of catalyst configuration and emphasized the electronic effect at the O–M contact interface [18]. In a later study by Qian et al., this effect was defined as electronic oxide-metal interaction (EOMI) [19]. Subsequently, a series of inverse catalysts (CeO₂/Cu [20], CeO₂/Pt [21], MgO/Au [22], CeO₂/Au [22], TiO₂/Au [22], ZnO/Cu [23], FeO_x/Rh [24], and SnO_x/Cu [25]) were successively explored, showing high catalytic properties and specific OMI, differing from the M/O supported (forward) catalysts.

The catalysts used in CO₂ methanation are usually supported catalysts [26], of which Ni-based catalysts, including Ni/ZrO₂ [27], Ni/CeO₂ [28], and Ni/Al₂O₃ [29], are the most widely used with the advantages of low cost and good performance. Although there are observations of the contributions of the M/O interfaces to catalytic performances and even the formation of new interfaces due to the SMSI phenomenon [30, 31], the detailed catalytic functions have not been well-clarified.

In this work, we have designed and synthesized an inverse CeO₂-Cr₂O₃/Ni model catalyst with preset O–M interface structure (CeO₂-Ni and Cr₂O₃-Ni) to investigate the effect of O–M interfaces on the catalyst performances in CO₂ methanation. CeO₂-Cr₂O₃/Ni shows a higher CO₂ methanation activity than the Ni nanoparticles, CeO₂/Ni, Cr₂O₃/Ni, and the physically mixed CeO₂/Ni+Cr₂O₃/Ni catalysts. In situ diffuse reflectance infrared Fourier transform spectroscopy (in situ DRIFTS) results and density functional theory (DFT) calculations suggest that CO₂ prefers to hydrogenate to HCOO* at CeO₂-Ni interfaces to produce CH₄ via the formate pathway, while at Cr₂O₃-Ni interfaces, CO₂ tends to decompose to CO* via the CO pathway. Introducing the Cr₂O₃-Ni interface to the CeO₂-Ni system brings an additional intermediate pathway (CO pathway), which shows the relatively lower adsorption energy of CO₂ and activation energy barrier of further dissociation, increasing the CO₂ adsorption and further conversion at low temperatures.

2. Experimental section

2.1. Chemicals and materials

The chemicals of analytical grade, including magnesium nitrate hexahydrate (Mg(NO₃)₂·6 H₂O, purity > 99.0%), nickel nitrate hexahydrate (Ni(NO₃)₂·6 H₂O, purity > 99.0%), cerium nitrate hexahydrate (Ce(NO₃)₃·6 H₂O, purity > 99.0%), and chromium nitrate nonahydrate (Cr(NO₃)₃·9 H₂O, purity > 99.0%), were purchased from Sinopharm Chemical Reagent Co., Ltd., China and were used without further

treatment.

2.2. Synthesis of materials

2.2.1. Synthesis of Ni(OH)₂

The Ni(OH)₂ nanosheets were synthesized via a modified ion exchange method, which was reported previously [32]. In a typical synthesis, Ni(NO₃)₂·6 H₂O (14.5 g) was dissolved in deionized water (100 mL) under stirring, followed by immersing MgO (1.60 g) as an alkali source to form a suspension. The MgO powder was obtained by calcinating Mg(NO₃)₂·6 H₂O. After stirring (500 r min^{−1}) for 48 h at 30 °C, the light green products of Ni(OH)₂ were separated by filtration, washed with deionized water several times, and dried at 100 °C overnight. The collected solid was denoted as Ni(OH)₂, as the content of Mg was measured to be 0.41 wt% only by ICP-OES.

2.2.2. Synthesis of catalysts

The as-prepared Ni(OH)₂ (0.9 g) was added into 60 mL of an aqueous solution containing Ce(NO₃)₃·6 H₂O (0.26 g) and Cr(NO₃)₃·9 H₂O (0.24 g) under stirring at 500 r min^{−1} until the suspension was formed. Then, the mixture was transferred to a 100-mL Teflon-lined stainless-steel autoclave and maintained at 120 °C for 12 h. The ion exchange process was driven by the difference in the product solubility (K_{sp}), in which NiCeCr mixed metal hydroxide (MMH) was in situ generated. After cooling to room temperature, the resulting precipitation was collected by filtration and washed with deionized water several times. Finally, the obtained solid was dried at 100 °C overnight and denoted as NiCeCr-MMH. NiCe-MMH and NiCr-MMH were prepared by a similar procedure, except that Cr(NO₃)₃·9 H₂O or Ce(NO₃)₃·6 H₂O were not added into the aqueous solution and the hydrothermal treatment for NiCe-MMH was maintained at 100 °C for 4 h.

The Ni(OH)₂, NiCr-MMH, NiCe-MMH, and NiCeCr-MMH were then calcinated at 500 °C for 2 h (Fig. S1a), resulting in the formation of NiO NPs, Cr₂O₃/NiO, CeO₂/NiO, and CeO₂-Cr₂O₃/NiO, respectively. Subsequently, the four catalysts were further reduced in H₂ with the flow rate of 50 mL min^{−1} at 450 °C for 2 h, yielding the reduced catalysts denoted as Ni NPs, Cr₂O₃/Ni, CeO₂/Ni, and CeO₂-Cr₂O₃/Ni, respectively.

The CeO₂/Ni+Cr₂O₃/Ni catalyst was obtained by physically mixing CeO₂/Ni (0.10 g) and Cr₂O₃/Ni (0.10 g) well with a mortar and pestle.

2.3. Characterization

The samples were characterized by using various methods, including scanning electron microscopy (SEM), transmission electron microscopy (TEM), X-ray diffraction (XRD), X-ray photoelectron spectroscopy (XPS), Raman spectra, N₂ adsorption/desorption, inductively coupled plasma optical emission spectrometer (ICP-OES), Thermogravimetric (TG) analysis, H₂ temperature-programmed reduction (H₂-TPR), H₂ temperature-programmed desorption (H₂-TPD), CO₂ temperature-programmed desorption (CO₂-TPD), and in situ diffuse reflectance infrared Fourier transform spectroscopy (in situ DRIFTS). Detailed procedures are provided in [Supporting Information](#).

2.4. Catalytic measurement

The catalytic activity test was carried out in a fixed bed reactor equipped with a quartz tube (I.D. 8 mm) at 0.1 MPa, in which the thermocouple was inserted into the furnace chamber to control the reaction temperature. A small amount of screened catalyst was used, and some quartz wools were packed on the top of the bed as the gas distributor. Additionally, the catalyst bed (catalyst diluted with quartz sand) was planted in the flat-temperature zone of the furnace, and the addition of the quartz sands was to avoid the generation of hotspots in the catalyst bed. Moreover, another thermocouple was inserted into the catalyst bed with a casing pipe to measure its temperature. The above measures could effectively eliminate the influences of mass and heat

transfers in the catalytic tests. In the activity test, typically, 0.2 g catalyst (20–40 mesh) diluted with 5.0 g quartz sand (20–40 mesh) was uploaded to a quartz tube with a height of ca. 6 cm, and the gas flow rate was 100 mL min⁻¹, corresponding to a weight hourly space velocity of 30000 mL g⁻¹ h⁻¹. First, the catalyst was reduced at 450 °C in pure H₂ (50 mL min⁻¹) for 2 h and then cooled to the starting reaction temperature in H₂. Then, the mixed CO₂ and H₂, as well as N₂ (as an internal standard), were introduced into the reactor at a molar ratio of CO₂/H₂/N₂ = 18/72/10 (100 mL min⁻¹) to investigate the catalytic activity of the catalysts at 230–450 °C. The temperature-programmed heating rate was set at 5 °C min⁻¹ in the whole temperature range. The experimental data were acquired after a 1 h reaction to obtain the steady-state result. Inlet and outlet gases were analyzed online by a Micro GC 3000 A (Fusion, INFICON) equipped with a TCD. In addition, a 100 h lifetime test of CO₂ methanation was performed at 310 °C, 0.1 MPa, 30000 mL g⁻¹ h⁻¹. The CO₂ conversion, CH₄ selectivity, and CH₄ yield are defined as follows [33]:

$$\text{CO}_2 \text{ conversion} = \frac{V_{\text{CO}_2, \text{in}} - V_{\text{CO}_2, \text{out}}}{V_{\text{CO}_2, \text{in}}} \times 100\% \quad (1)$$

$$\text{CH}_4 \text{ selectivity} = \frac{V_{\text{CH}_4, \text{out}}}{V_{\text{CO}_2, \text{in}} - V_{\text{CO}_2, \text{out}}} \times 100\% \quad (2)$$

$$\text{CH}_4 \text{ yield} = \text{CO}_2 \text{ conversion} \times \text{CH}_4 \text{ selectivity} \times 100\% \quad (3)$$

where $V_{\text{CO}_2, \text{in}}$ and $V_{\text{CO}_2, \text{out}}$ are the volume flow rates of CO₂ at the inlet and outlet of the reactor at standard temperature and pressure (STP), mL min⁻¹.

The normalized rate and activation energy for CO₂ methanation over the catalysts were measured at 0.1 MPa with a catalyst loading of 0.2 g (20–40 mesh) diluted with 5.0 g quartz sand (20–40 mesh). The experiments were performed at different total gas flow rates of 50, 100, and 150 mL min⁻¹ at temperatures of 200, 210, 220, and 230 °C to lower the CO₂ conversion to the range of 1–20%. The moles of CO₂ consumed per mass of catalyst (Rate_m) were determined using the following equation [33]:

$$\text{Rate}_m \text{ (mol} \cdot \text{g}_{\text{cat}}^{-1} \cdot \text{s}^{-1}) = \frac{F_{\text{CO}_2} \bullet \text{CO}_2 \text{ conversion}}{W} = \frac{\text{CO}_2 \text{ conversion}}{W/F_{\text{CO}_2}} \quad (4)$$

where F_{CO_2} represents the flow of CO₂ in mol min⁻¹ and W is the weight of the catalyst in g. The variations in CO₂ conversion with respect to W/F_{CO_2} were plotted, and then the rates of reaction were calculated at various temperatures according to the slope of the linear portion. (The "linear portion" means a straight line fitted by three points (Fig. S2)). The activation energy was calculated using the Arrhenius equation.

2.5. Computational methods and models

All the periodic DFT calculations were carried out using the Vienna ab initio simulation package (VASP) [34,35]. The core electrons were treated with the projector augmented-wave (PAW) pseudopotentials. The exchange-correlation function was described by generalized gradient approximation (GGA) using Perdew-Burke-Ernzerhof (PBE) function [36]. The plane-wave cutoff energy was set as 450 eV, the Monkhorst-Pack k-point was set as Gamma point, and the $U_{\text{eff}} = 5.0$ eV was applied to the Ce 4 f states [37]. The convergence criterion for the geometric relaxation was 0.02 eV/Å. The transition states for all the elementary reactions were searched using the CI-NEB method [38]. The adsorption energy was calculated using the following equation: $E_{\text{ads}} = E_{\text{mol/sur}} - (E_{\text{mol}} + E_{\text{sur}})$. $E_{\text{mol/sur}}$ represents the energy of the total adsorbed system, E_{mol} is the energy of a free molecule in the gas phase, and E_{sur} represents the energy of the catalyst surface. The reaction barrier was calculated through the subsequent equation: $E_a = E_{\text{TS}} - E_r$. The E_{TS} and E_r represent the energies of transition states and reactants, respectively.

The CeO₂/Ni and Cr₂O₃/Ni models were constructed based on the Ni (111) surface. In detail, the CeO₂ and Cr₂O₃ clusters were generated from the CeO₂ (111) and Cr₂O₃ (001) surfaces. After that, the clusters were loaded on the three-layer (4 × 4) Ni (111) surface, as shown in Fig. S3. The atoms in the bottom two layers were fixed, while the rest were relaxed. The vacuum region was set as 13 Å.

3. Results and discussion

3.1. Characterization of the catalysts

3.1.1. SEM and TEM analyses

Fig. 1 exhibits the SEM images of all the samples. The as-prepared NiCeCr-MMH, NiCe-MMH, and NiCr-MMH all show a morphology of small sandwich-like nanosheets with a diameter of approximately 100–200 nm (Fig. 1a–c), while Ni(OH)₂ exists as monolayer sheets (Fig. 1d). After calcination, the obtained CeO₂-Cr₂O₃/NiO retains the major lamellar structure with relatively smooth surfaces (Fig. 1e). CeO₂/NiO and Cr₂O₃/NiO almost maintain their original structure of nanosheets but with rougher surfaces (Fig. 1f and g), while NiO (Fig. 1h) no longer remains the sheet structure. After reduction, the morphology of all catalysts transformed into closely connected particles (as observed in Fig. 1i–l), with the three catalysts exhibiting comparable particle sizes.

Fig. 2 shows the TEM images of the Ni-supported oxide inverse catalysts and Ni NPs. For Cr₂O₃/Ni (Fig. 2a and b), the observed lattice distance of 0.204 nm corresponds to the (111) facet of Ni, and the lattice distance of 0.145 nm originates from the (300) facet of Cr₂O₃ [39,40]. In the HRTEM images of CeO₂/Ni (Fig. 2c and d), CeO₂ mainly exposes the (111) and (200) facets corresponding to the lattice distance of 0.311 and 0.267 nm, respectively, and the Ni particles also expose (111) facet with a lattice distance of 0.204 nm [11]. In the zoomed TEM images (Fig. 2b, d), the single CeO₂-Ni and Cr₂O₃-Ni interfaces can be observed clearly on the CeO₂/Ni and Cr₂O₃/Ni surfaces (line in Fig. 2a, c). Notably, for CeO₂-Cr₂O₃/Ni, the Ni (111), CeO₂ (111), and Cr₂O₃ (300) facets could be observed, demonstrating the Ni particles are decorated with CeO₂ and Cr₂O₃ islands, which generate two kinds of interfaces between Ni and CeO₂ or Cr₂O₃ (line in Fig. 2e–g). As demonstrated later, forming CeO₂-Ni and Cr₂O₃-Ni can facilitate charge transfer. In short, oxide/Ni inverse catalysts can be synthesized successfully via in situ ion exchange, which possesses many contacted oxide-metal interfaces.

3.1.2. XRD, H₂-TPR, H₂-TPD, and CO₂-TPD analyses

The XRD patterns of all the catalysts are shown in Fig. 3. For Ni NPs, three strong diffraction peaks are observed at 2θ of 44.51, 51.85, and 76.37° (Fig. 3a), corresponding to the (111), (200), and (220) facets of Ni (JCPDS 04–0850) [28]. For Cr₂O₃/Ni, only Ni peaks are observed. For CeO₂/Ni, besides the Ni peaks, a series of weak CeO₂ peaks (JCPDS 43–1002) are also observed. For CeO₂-Cr₂O₃/Ni, both the strong Ni and weak CeO₂ peaks are observed. Noteworthy, we only observe the weak signals of CeO₂ but no signal of Cr-related species in all the Ce/Cr-containing catalysts, attributed to their low content (Fig. 3a) [28]. Fig. 3b shows the enlarged XRD patterns in the range of 2θ = 43–46°, revealing weaker and wider Ni (111) diffraction peaks than those of Ni NPs in Cr₂O₃/Ni, CeO₂/Ni, and CeO₂-Cr₂O₃/Ni, meaning that introducing oxides, especially dual metal oxides, to construct oxide-metal interfaces can reduce the Ni particle size and improve their dispersion. The Ni crystal sizes calculated by the Scherrer formula and surface areas from N₂ adsorption/desorption are listed in Table 1, in which the three Ni-supported oxide inverse catalysts exhibit a similar but larger special surface area than the Ni NPs. The slight 2θ shift observed for both the CeO₂-Cr₂O₃/Ni and Cr₂O₃/Ni indicates that a small part of the Cr ions entered the Ni lattice and increased the lattice distances [41].

Fig. 4a presents the H₂-TPR profiles of all the samples, which reflect the reducibility and metal-oxide interaction of the catalysts. For NiO NPs, one main reduction peak is observed at 335 °C, which can be

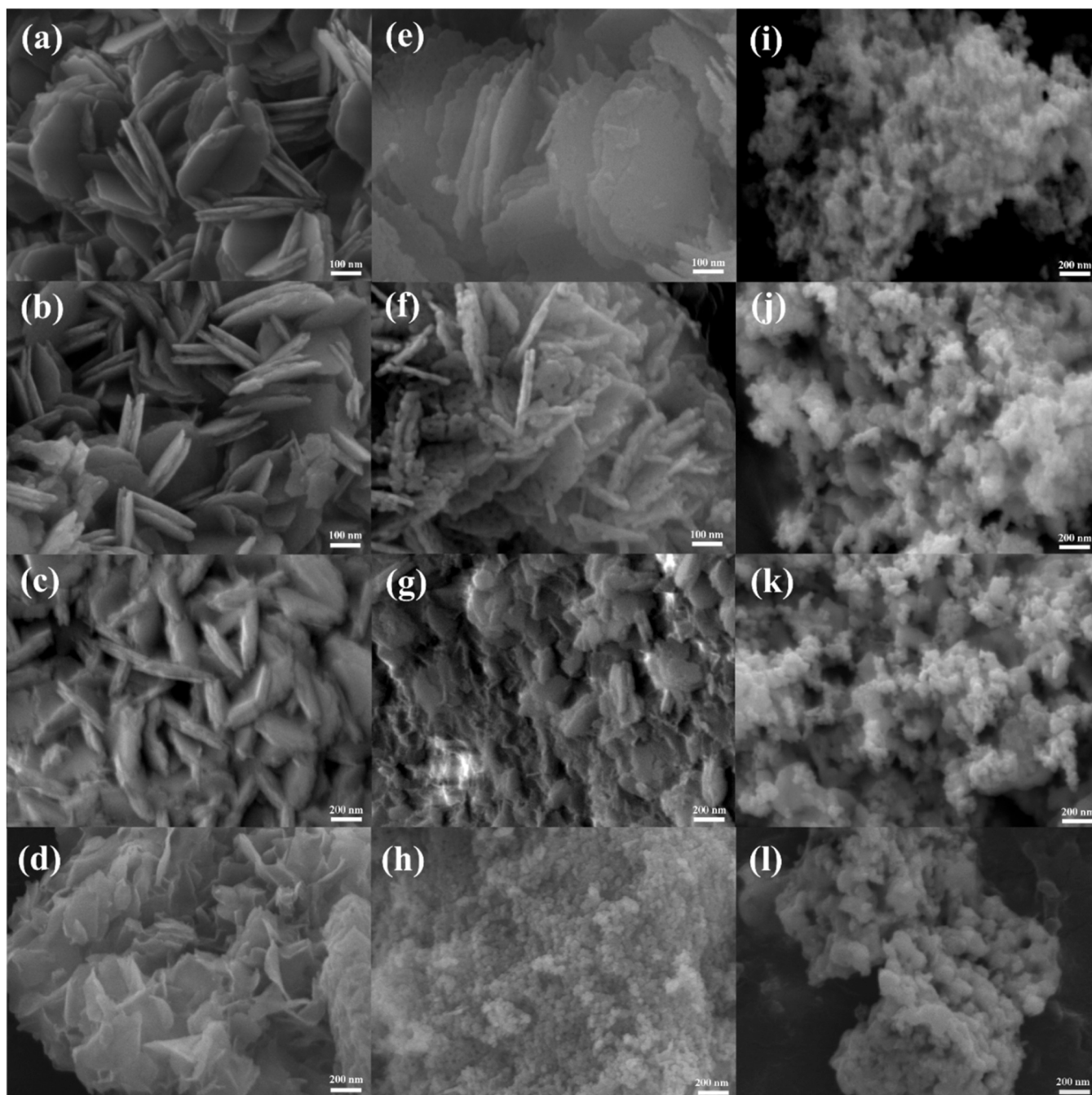


Fig. 1. SEM images of NiCeCr-MMH (a), NiCe-MMH (b), NiCr-MMH (c), Ni(OH)₂ (d), CeO₂-Cr₂O₃/NiO (e), CeO₂/NiO (f), Cr₂O₃/NiO (g), NiO NPs (h), CeO₂-Cr₂O₃/Ni (i), CeO₂/Ni (j), Cr₂O₃/Ni (k), and Ni NPs (l).

ascribed to the reduction of Ni²⁺ species. For Cr₂O₃/Ni, the main hydrogen consumption peak shifts to a higher temperature (~470 °C), assigned to the NiO species that strongly interacted with the Cr oxides [42]. Compared with Cr₂O₃/Ni, the profile of CeO₂/Ni presents a peak at a lower temperature of 445 °C, suggesting a relatively weaker metal-oxide interaction [28]. For CeO₂-Cr₂O₃/Ni, the main peak is located at 456 °C, which is higher than that of CeO₂/Ni but lower than that of Cr₂O₃/Ni, indicating the synergistic interactions of Ce-Cr-coexistence with the Ni species, providing evidence for the possible formation of the CeO₂-Ni and Cr₂O₃-Ni interfaces. The calculated H₂ consumption based on the main peaks below 470 °C is listed in Table 1, in which the slightly lower H₂ consumption amount of CeO₂-Cr₂O₃/Ni than CeO₂/Ni can be attributed to its relatively small Ni crystal size. Considering the different reduction levels (Fig. S1b and c),

the calcinated catalysts were reduced at 450 °C for 2 h, which would enable the reduction of the majority of the Ni species (as shown in Fig. 3) but have no big influence on the Cr and Ce oxides. Additionally, the higher reduction peak temperature observed for oxide/Ni samples compared to bulk NiO suggests the modification of NiO by surface oxides, resulting in the formation of superficial oxide-Ni interactions. This is further supported by the XPS and ICP results.

Fig. 4b shows the H₂-TPD profiles of all the catalysts. Generally, one or two desorption peaks are observed in the temperature range of 80–200 °C, corresponding to the chemisorbed hydrogen on the sufficiently exposed Ni surface. The integral areas of these peaks follow the order of CeO₂-Cr₂O₃/Ni > CeO₂/Ni > Cr₂O₃/Ni, indicating the best capability of CeO₂-Cr₂O₃/Ni to adsorb molecular hydrogen. Moreover, CeO₂-Cr₂O₃/Ni possesses the highest H₂ uptake of 321.5 μmol g⁻¹

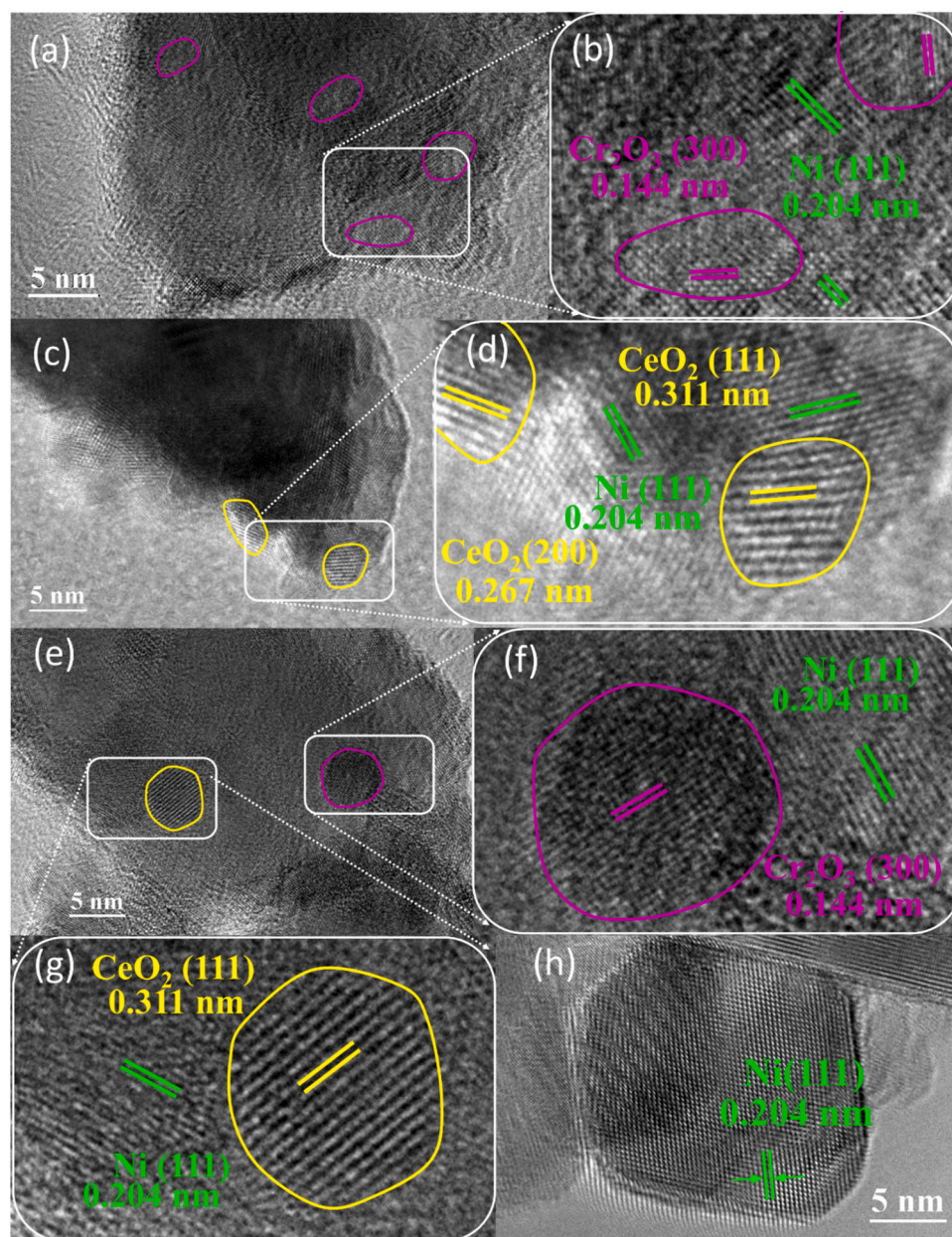


Fig. 2. HRTEM images of $\text{Cr}_2\text{O}_3/\text{Ni}$ (a and b), CeO_2/Ni (c and d), $\text{CeO}_2\text{-Cr}_2\text{O}_3/\text{Ni}$ (e-g), and Ni NPs (h).

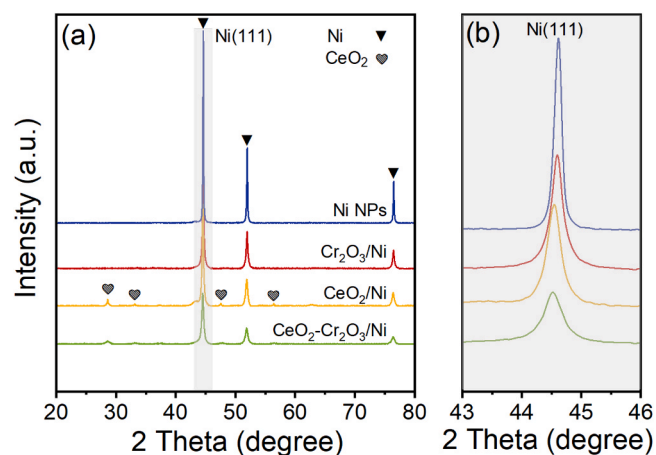


Fig. 3. XRD patterns of the catalysts (a) and partially magnified profiles (b).

Table 1

Physical and chemical properties of the catalysts after reduction.

Catalysts	Ni crystal size ^a (nm)	Surface area ^b ($\text{m}^2 \text{g}^{-1}$)	H_2 consumption ^c (mmol g^{-1})	H_2 uptake ^d ($\mu\text{mol g}^{-1}$)
Ni NPs	49.02	12	10.0	126.7
$\text{Cr}_2\text{O}_3/\text{Ni}$	25.96	24	12.3	161.4
CeO_2/Ni	23.38	27	21.7	237.8
$\text{CeO}_2\text{-Cr}_2\text{O}_3/\text{Ni}$	19.65	29	21.0	321.5

^a Ni crystal size, calculated via Scherrer formula based on Ni(111) peak.

^b Surface area, derived from BET equation,

^c H_2 consumption, calculated based on the H_2 -TPR results and calibrated by the reduction of the CuO standard sample,

^d H_2 uptake, calculated based on H_2 -TPD results,

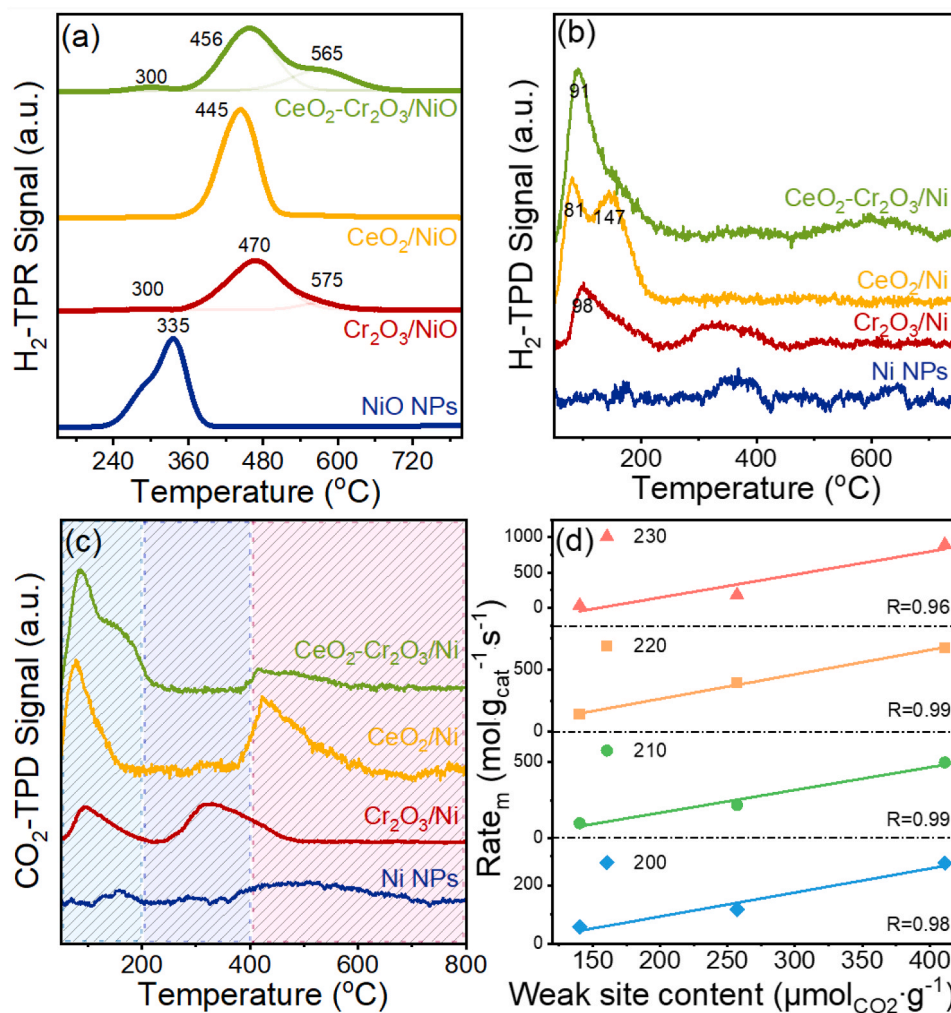


Fig. 4. (a) H₂-TPR profiles of all the catalysts before reduction; (b) H₂-TPD profiles and (c) CO₂-TPD profiles of all the catalysts after the reduction; (d) relationship between the reaction rate and weak site content.

(Table 1) due to the appropriate metal-oxide interfacial interaction, which results in the exposure of abundant metal sites segregated by Ce-Cr-oxides [43].

Fig. 4c shows the CO₂-TPD profiles of all the reduced catalysts. The CO₂-desorption curves are categorized into three regions within the investigated temperature range, namely 50–200, 200–400, and > 400 °C, corresponding to the presence of the weak, medium, and strong basic sites, respectively [40]. The CO₂ molecules adsorbed on the weak and medium basic sites should be relatively active in CO₂ methanation, especially the weak basic sites [44,45]. The relative content of CO₂ absorption at different basic sites is listed in Table 2. The desorption amount of CO₂ on the weak basic sites over CeO₂-Cr₂O₃/Ni is about 1.6 times and 4.0 times higher than those on CeO₂/Ni and Cr₂O₃/Ni, respectively, despite its total amount is not the highest, providing evidence for its excellent CO₂ adsorption and conversion. It

can also be observed that the amount of medium and strong basic sites decreased after the introduction of Cr₂O₃ into CeO₂/Ni, probably attributed to the modulation of the outer electron distribution of Ni by the introduction of Cr₂O₃ [46,47], and this deduction can be further confirmed by the following XPS results. To further determine the influence of weak basic sites, the relationship between the mole conversion of CO₂ per mass of catalyst and weak basic site content was plotted, as shown in Fig. 4d. A high relevance exists in these parameters at 200–250 °C of which the R values reach 0.96–0.99, indicating the weak basic sites indeed play a significant role in the CO₂ activation at low temperatures.

3.1.3. XPS and Raman analyses

The chemical states of the various elements in the reduced catalysts were studied using XPS technology to quantitatively estimate the oxygen vacancy (O_v) concentrations and deduce the charge transfer. Fig. 5a presents the O 1s spectra of the three oxide/Ni inverse catalysts. The peak at 529.4 eV is ascribed to lattice oxygen species (O_{latt}) of metal oxides, and those located at 530.9–531.2 eV are related to surface-adsorbed oxygen (O_{ads}), while the peak at 532.7–533.7 eV corresponds to the oxygen of adsorbed water (O_{wat}) [48–50]. The content of adsorbed oxygen species can reflect the amount of O_v. The area of O_{ads} over CeO₂-Cr₂O₃/Ni is obviously larger than that over CeO₂/Ni and Cr₂O₃/Ni. Relatively, the O_{ads}/(O_{ads} + O_{latt}) molar ratios were calculated to estimate the oxygen vacancy concentrations on the surface of

Table 2
CO₂-TPD results of the catalysts after reduction.

Catalysts	CO ₂ desorption (μmol _{CO2} g _{cat} ⁻¹)			
	Weak (< 200 °C)	Medium (200–400 °C)	Strong (> 400 °C)	Total
Cr ₂ O ₃ /Ni	104.3	156.3	37.3	297.9
CeO ₂ /Ni	257.0	37.7	312.5	607.2
CeO ₂ -Cr ₂ O ₃ /Ni	411.1	24.2	103.7	539.0

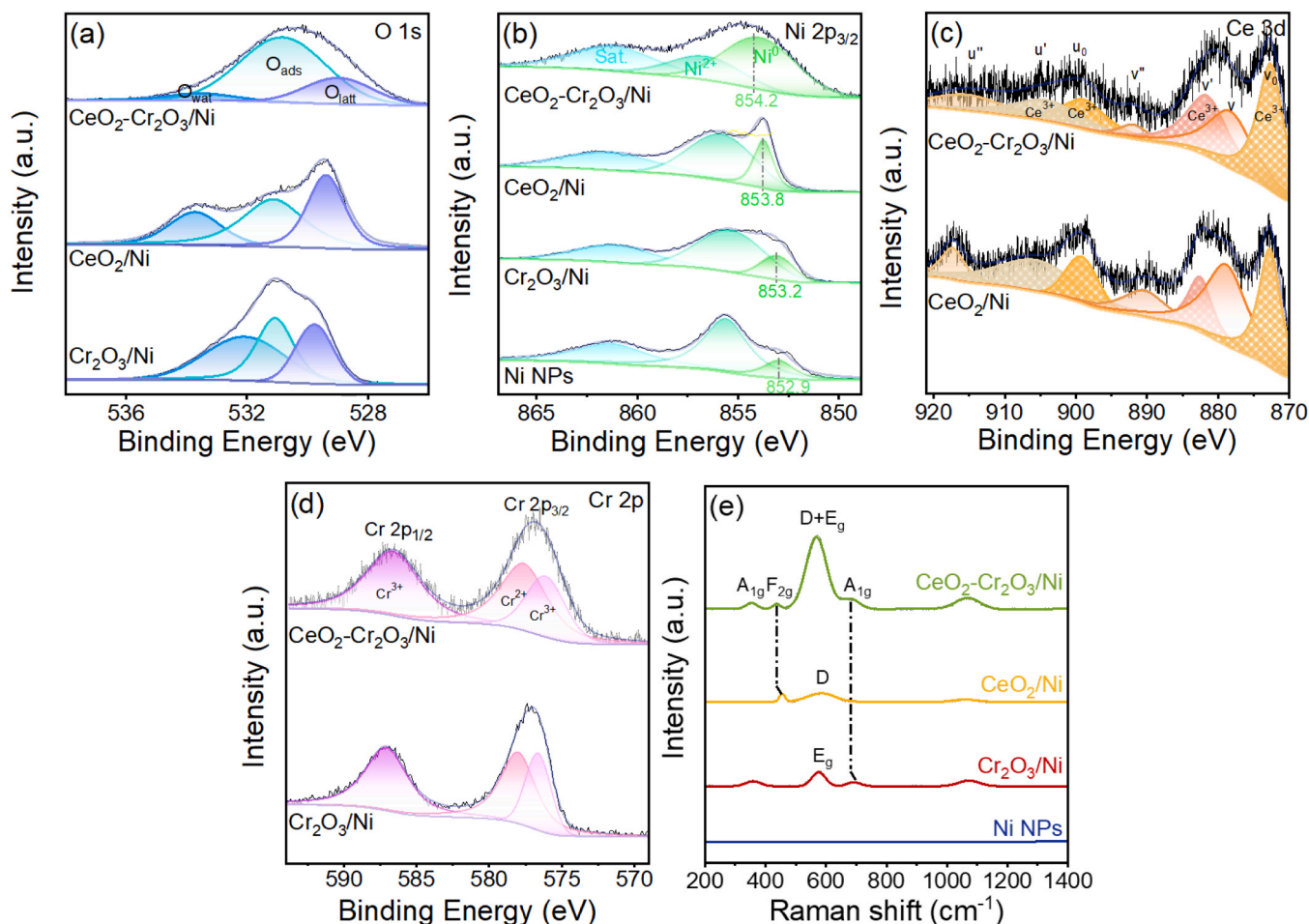


Fig. 5. XPS spectra of O 1s (a), Ni 2p (b), Ce 3d (c), and Cr 2p (d), and Raman spectra (e) of the catalysts.

these catalysts, which follow the order of $\text{CeO}_2\text{-Cr}_2\text{O}_3/\text{Ni}$ (75.6%) > CeO_2/Ni (49.3%) > $\text{Cr}_2\text{O}_3/\text{Ni}$ (34.2%), proving that $\text{CeO}_2\text{-Cr}_2\text{O}_3/\text{Ni}$ indeed possesses the largest amount of oxygen vacancies. Moreover, the oxygen atoms can be removed from the interfacial sites to form oxygen vacancies with much lower energy than at other regions of the surface [2,51]. The higher O_v content implies a higher content of low oxygen coordination defect sites [52], thus activating adsorbed oxygen and providing a lattice position for oxygen migration and facilitating electron transfer [53].

Fig. 5b shows the Ni 2p spectra of all the catalysts. The Ni 2p peaks at 853.8–854.5 eV and 855.5–856.7 eV are attributed to Ni^0 and Ni^{2+} species, and the peaks at 861.0–861.5 eV to the satellite peaks [40]. Theoretically, electronic interfacial interactions usually occur between adjacent components in heterogeneous catalysts, and the electron transfer phenomenon exists between metal and semiconductor oxide with differential work functions [54]. Compared with Ni NPs, large range shifts of Ni⁰ binding energy are observed for the oxide/Ni inverse catalysts, indicating that the electron distribution state of Ni is regulated by Ce-oxides and/or Cr-oxides [55]. In particular, compared to the binding energy of Ni NPs, those of CeO_2/Ni , $\text{Cr}_2\text{O}_3/\text{Ni}$ and $\text{CeO}_2\text{-Cr}_2\text{O}_3/\text{Ni}$ shift by 0.3, 0.9, and 1.3 eV, respectively, toward the high energy direction, demonstrating the decrease in electronic cloud density of Ni and the propensity to lose electrons. These results confirm that adding Cr/Ce oxides improves electron transfer by forming an additional Ni-oxide interface. Using an inversely loaded catalyst with a metal substrate (oxide/Ni) is advantageous as the high content Ni has abundant electrons that can easily donate to the small amount of semiconductor oxide component [1,18]. In contrast, traditional oxide-supported catalysts

(Ni/oxide) have low Ni contents, making it difficult to donate electrons under the electronic concentration equilibrium [56].

The Ce 3d spectra can be deconvoluted into seven peaks (Fig. 5c). The four peaks denoted by u_0 , u' , v_0 and v' are assigned to surface Ce^{3+} , and the peaks denoted by u'' , v , and v'' to surface Ce^{4+} [56]. The $\text{Ce}^{3+}/(\text{Ce}^{3+} + \text{Ce}^{4+})$ ratios were calculated and listed in Table 3. For $\text{CeO}_2\text{-Cr}_2\text{O}_3/\text{Ni}$ and CeO_2/Ni , the surface ratios of $\text{Ce}^{3+}/(\text{Ce}^{3+} + \text{Ce}^{4+})$ are calculated to be 61.2% and 60.3%, respectively. These results indicate that introducing Cr species results in more surface Ce^{3+} on $\text{CeO}_2\text{-Cr}_2\text{O}_3/\text{Ni}$.

For the Cr 2p spectra (Fig. 5d), the peaks at 576.1, 577.6, and 586.6 eV correspond to $2p_{3/2}$ and $2p_{1/2}$ of Cr^{3+} , and $2p_{1/2}$ of Cr^{2+} , respectively [41]. Previous reports have shown that the reduction temperature of the bulk phase CeO_2 [28] and Cr_2O_3 [42] are higher than that of the current catalyst (450 °C). Consequently, the presence of Cr^{2+} and Ce^{3+} , and the obvious shift of Ni^0 peak towards high binding energy in $\text{CeO}_2\text{-Cr}_2\text{O}_3/\text{Ni}$, suggest that there is a significant electron transfer from Ni^0 to Ce^{4+} as well as Ni^0 to Cr^{3+} through Ni–O–Ce and Ni–O–Cr

Table 3

The quantitative analyzing results of the catalyst surfaces by XPS.

Catalysts	$\text{O}_{\text{ads}} (\text{O}_{\text{ads}} + \text{O}_{\text{lat}})$ molar ratio (%)	$\text{Ce}^{3+}/(\text{Ce}^{3+} + \text{Ce}^{4+})$ molar ratio (%)	Ni^0 binding energy (eV)
Ni NPs	N/A	N/A	852.9
$\text{Cr}_2\text{O}_3/\text{Ni}$	34.2	N/A	853.2
CeO_2/Ni	49.3	60.2	853.8
$\text{CeO}_2\text{-Cr}_2\text{O}_3/\text{Ni}$	75.6	61.3	854.2

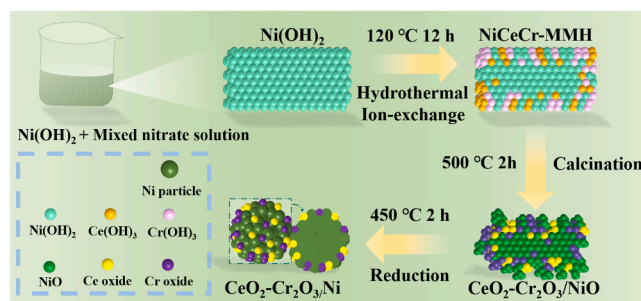
bridging oxygen bonds, leading to the generation of Ce^{3+} and Cr^{2+} [57]. From the surface and bulk components of the catalysts by XPS and ICP-OES (Table 4), it can be observed that the surface Ni content is lower than that of the bulk phase, while the surface Ce and Cr content is higher than that of the bulk phase, indicating that the Ce/Cr oxides mostly covered on the surface of Ni.

The Raman spectra of the four catalysts are shown in Fig. 5e, and the Raman peak assignments are listed in Table S1, which exhibit obvious differences among these catalysts. The peak at 1065 cm^{-1} is caused by the quartz glass in the test [58]. For Ni NPs, no peak can be observed. For $\text{Cr}_2\text{O}_3/\text{Ni}$, the peaks located at 351 and 690 cm^{-1} are assigned to the A_1g mode, and that located at 575 cm^{-1} to the E_g mode of Cr–O [59]. For CeO_2/Ni , a peak located at 449 cm^{-1} can be attributed to the F_2g octahedrally symmetrical vibration mode of Ce–O [60], and the coexistence of 449 cm^{-1} and 571 cm^{-1} could be referred to the presence of Ni–O–Ce bonds [61]. For $\text{CeO}_2\text{-Cr}_2\text{O}_3/\text{Ni}$, two shifts of 449 cm^{-1} to 439 cm^{-1} and 690 cm^{-1} to 677 cm^{-1} are observed, indicating that electron transfer occurs from Ni through Ni–O–Ce and Ni–O–Cr bonds [62]. The D mode represents the surface defects, such as O_v [63]. Even though the D and the E_g modes of Cr–O overlap, it is not difficult to see that the Raman spectrum of $\text{CeO}_2\text{-Cr}_2\text{O}_3/\text{Ni}$ shows a significantly high intensity of D mode, proving the abundant surface defects on it, i.e., with a sufficiently high content of oxygen vacancies, which is consisted with the XPS results (Fig. 5a). Thus, combining the results of H_2 -TPR, XPS, and Raman, we deduce that the Ce/Cr oxides mostly embedded on the surface of Ni in the $\text{CeO}_2\text{-Cr}_2\text{O}_3/\text{Ni}$ samples synthesized by in situ ion-exchange. The formed $\text{Cr}_2\text{O}_3\text{-Ni}$ interfaces change the electron distribution of Ni, then indirectly modifying the electronic structure of the nearby $\text{CeO}_2\text{-Ni}$ interfaces. The two kinds of interfaces cooperatively facilitate rapid electron transfer.

3.1.4. Formation of $\text{CeO}_2\text{-Cr}_2\text{O}_3/\text{Ni}$

According to the characterizations above, the synthesis process of the oxide/Ni inverse catalysts with the contacted O–M interfaces can be schematically illustrated in Scheme 1. Firstly, the $\text{Ni}(\text{OH})_2$ precursor is added into the solution containing Cr^{3+} and Ce^{3+} ; then the ion exchange occurs by replacing Ni^{2+} with Cr^{3+} and Ce^{3+} on the surface of $\text{Ni}(\text{OH})_2$ to form an in situ-generated NiCeCr-MMH . After the calcination, the mixed metal hydroxides evolve into the mixed metal oxides with a morphology of rough nanosheets, where the escape of water leads to surface porosity and unevenness. After the reduction by H_2 , the porous and uneven nanosheets break into smaller particles, while metallic Ni particles are generated with the formation of $\text{CeO}_2\text{-Ni}$ and $\text{Cr}_2\text{O}_3\text{-Ni}$ interfaces. It should be noted that the precursors of Ni and Ce or Cr oxides are both hydroxides that undergo a similar evolution to form abundant and close-contact oxide (CeO_2 and Cr_2O_3)-Ni interfaces in situ.

Based on the discussions above, we used a mildly inverse ion-exchange method to artificially cover the Ni nanoparticle with oxide, modeling the uncontrollable high temperature-induced oxide overlayer on Ni in the supported catalysts. The hypothesized structure of the model catalyst has been confirmed and allowed to reveal the roles of various O–M interfaces in CO_2 methanation. The controllable ion exchange driven by product solubility can lead to in situ formation of small amounts of inversely loaded oxide. Namely, the individual Ni particles



Scheme 1. Schematic illustration of the synthesis process of $\text{CeO}_2\text{-Cr}_2\text{O}_3/\text{Ni}$.

are modified by surface oxides, which are in situ generated on Ni, to eliminate the effect of support and to generate and magnify EOMI. In this way, it not only can avoid the uncontrollable high-temperature reduction needed to form the new O/M interface surfaces via SMSI but also provide a clear view of the O–M interface from a different perspective employing the designed new interface structures.

3.2. Catalytic performance of catalysts

Fig. 6 exhibits the catalytic performance of the catalysts, in which the thermodynamic equilibrium data is obtained from our previous work [64]. For the five samples, the CO_2 conversions over them follow the order of $\text{CeO}_2\text{-Cr}_2\text{O}_3/\text{Ni} > \text{CeO}_2/\text{Ni} + \text{Cr}_2\text{O}_3/\text{Ni} > \text{CeO}_2/\text{Ni} > \text{Cr}_2\text{O}_3/\text{Ni} > \text{Ni NPs}$. Notably, at $290\text{ }^\circ\text{C}$, CO_2 conversion over $\text{CeO}_2\text{-Cr}_2\text{O}_3/\text{Ni}$ is about 1.3, 2.1, and 9.0 times higher than that over CeO_2/Ni , $\text{Cr}_2\text{O}_3/\text{Ni}$, and Ni NPs, respectively (Fig. 6a). Furthermore, the CO_2 conversion over $\text{CeO}_2\text{-Cr}_2\text{O}_3/\text{Ni}$ presents a trend of firstly increasing with reaction temperature to reach a thermodynamic equilibrium at $330\text{ }^\circ\text{C}$ and then gradually decreasing. The CeO_2/Ni and $\text{Cr}_2\text{O}_3/\text{Ni}$ show similar situations, but they reach thermodynamic equilibrium at a higher temperature ($350\text{ }^\circ\text{C}$ and $400\text{ }^\circ\text{C}$, respectively) compared to $\text{CeO}_2\text{-Cr}_2\text{O}_3/\text{Ni}$, indicating that the formation of such a special interface contact as well as the Cr-introduction improved the capability of $\text{CeO}_2\text{-Cr}_2\text{O}_3/\text{Ni}$ to overcome kinetic limitations. It can be seen that the mechanically mixed $\text{Cr}_2\text{O}_3/\text{Ni} + \text{CeO}_2/\text{Ni}$ catalysts exhibit better performance than single $\text{Cr}_2\text{O}_3/\text{Ni}$ and CeO_2/Ni , indicating an electronic modulation of $\text{Cr}_2\text{O}_3\text{-Ni}$ and $\text{CeO}_2\text{-Ni}$ interfaces, in agreement with the XPS results. And the better catalytic performance of $\text{CeO}_2\text{-Cr}_2\text{O}_3/\text{Ni}$ than the $\text{Cr}_2\text{O}_3/\text{Ni} + \text{CeO}_2/\text{Ni}$ catalyst also proves the advantage of in situ formation of the interfacial structures. Furthermore, $\text{CeO}_2\text{-Cr}_2\text{O}_3/\text{Ni}$ shows a higher CO_2 conversion than the Ni-based catalysts reported in the literature (Table S2). For CH_4 selectivity (Fig. 6b), all the catalysts keep $\sim 100\%$ above $270\text{ }^\circ\text{C}$. The CO selectivity was also calculated and is presented in Fig. S4, which indicates that all the oxide/Ni catalysts exhibit CO selectivity below 3% above $250\text{ }^\circ\text{C}$. However, compared to other catalysts, the Ni nanosheets exhibited extremely poor CH_4 selectivity below $270\text{ }^\circ\text{C}$, which further illustrates the importance of the O–M interface for improving the CH_4 selectivity at low temperatures. The CH_4 yield shows a similar trend to the CO_2 conversion (Fig. 6c). The durability of $\text{CeO}_2\text{-Cr}_2\text{O}_3/\text{Ni}$ was subsequently evaluated during a 100 h on-stream reaction at $310\text{ }^\circ\text{C}$ with the same condition of $30000\text{ mL g}^{-1}\text{ h}^{-1}$ (Fig. 6d). No manifest deactivation was observed after the 100 h test. The CH_4 selectivity was maintained at about 99%, and the CO_2 conversion declined by less than 4%. Furthermore, the XRD analysis (Fig. S5 and Table S3) reveals no significant change in the Ni particle size in the spent catalysts after the reaction or the life test. Moreover, the TG and XPS analyses (Fig. S5) show a final weight increase of 3.81% in the spent catalyst compared to the fresh one, along with a content change of Ni^0 . These results suggest that a higher content of Ce and Cr ions in low valence states was oxidized, indicating frequent electron transfer between Ni and Ce/Cr oxides during CO_2 methanation. The activation energies on the three catalysts were measured (Fig. 6e), and the

Table 4

The surface and bulk compositions of the catalysts.

Name		Ni (atom. %)	Ce (atom. %)	Cr (atom. %)
$\text{Cr}_2\text{O}_3/\text{Ni}$	surface ^a	32.42	N/A	7.41
	bulk ^b	86.79	N/A	2.96
CeO_2/Ni	surface ^a	31.27	1.23	N/A
	bulk ^b	87.89	1.05	N/A
$\text{CeO}_2\text{-Cr}_2\text{O}_3/\text{Ni}$	surface ^a	40.13	1.08	5.93
	bulk ^b	88.09	0.97	2.16

^a Obtained based on the XPS results,

^b Calculated based on the ICP-OES results.

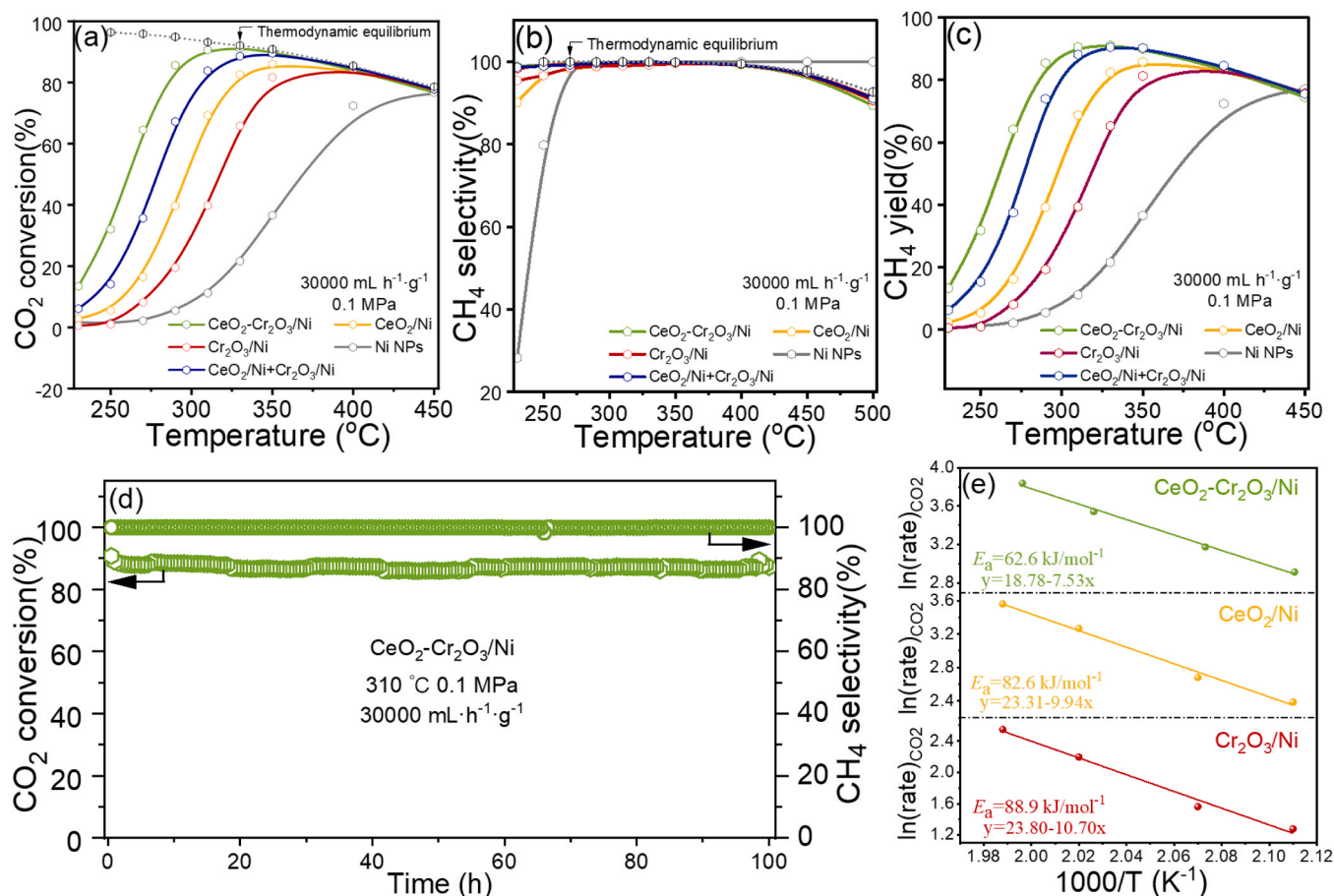


Fig. 6. Catalytic performance of the catalysts: (a) CO₂ conversion, (b) CH₄ selectivity, (c) CH₄ yield, (d) lifetime test, and (e) Arrhenius plot.

Arrhenius plots show that the activation energy follows the order of CeO₂-Cr₂O₃/Ni (62.6 kJ mol⁻¹) > CeO₂/Ni (82.6 kJ mol⁻¹) > Cr₂O₃/Ni (88.9 kJ mol⁻¹), which is consistent with the trend of their activities in CO₂ methanation (Fig. 6a).

3.3. In situ DRIFTS analysis

In situ DRIFTS investigation was conducted to study the active intermediates and the reaction mechanisms, and the band assignments are summarized in Table S4. The spectra recorded in the reaction gas (72% H₂/18% CO₂/10% N₂) at different temperatures (50–450 °C) on the three catalysts are shown in Fig. 7a-c. For CeO₂-Cr₂O₃/Ni (Fig. 7a), typical surface species like monodentate carbonates (1448 and 1513 cm⁻¹) [41,65] and bidentate carbonates (1569 cm⁻¹) [47] are observed at each temperature, with intensities increased then decreased with increasing temperature. Below 200 °C, the band of linear-CO* (2074 cm⁻¹) [66] can also be observed, and no significant band of HCOO* is observed. Based on the above results, it can be inferred that CO is formed by CO₂ rather than HCOO* when the temperature is below 200 °C [29]. Above 200 °C, the bands of *CHO (1740 cm⁻¹) [67], HCOO* (1340, 1395, and 1684 cm⁻¹), and CH₄ (3016 cm⁻¹) appear gradually [56], and the intensity of these bands increase with increasing temperature. The band intensity of CH₄ is far stronger than those of the other species, suggesting the rapid reaction rate on the interface-rich Ni catalysts. Similar trends were found on both CeO₂/Ni and Cr₂O₃/Ni. Besides, for CeO₂/Ni (Fig. 7b), when the temperature is lower than 350 °C, the peak intensity of linear-CO* is much lower than that of HCOO*, and the peak of linear-CO* gradually disappears with the increase in temperature, indicating that linear-CO* is the intermediate but mightily not dominate in the CH₄ production. For Cr₂O₃/Ni (Fig. 7c), the

band of linear-CO* (2077 cm⁻¹) is detected at all temperatures. Above 350 °C, weaker formate species (1340 cm⁻¹) are observed [68]. It is suggested that, at low temperatures, the CO pathway occurs mainly on Cr₂O₃/Ni. The above results reveal that CeO₂-Cr₂O₃/Ni has a larger capacity for adsorbing CO₂ to decompose into the intermediate of CO* or hydrogenating CO₂ to the intermediate of HCOO*, but both are active intermediates to the product CH₄.

To further investigate the evolution of carbon species on the three catalysts, in situ DRIFTS spectra were recorded at 310 °C by switching the inlet gas from 72% H₂/18% CO₂/10% N₂ to 10% H₂/N₂. For CeO₂-Cr₂O₃/Ni (Fig. 7d), when the inlet gas is 72% H₂/18% CO₂/10% N₂, the bands of HCOO* (1368 and 1307 cm⁻¹), *CHO (1730 cm⁻¹), and monodentate carbonate (1516 cm⁻¹) are observed, along with the generation of CH₄ (3017 cm⁻¹). Furthermore, the band of linear-CO* (2070 cm⁻¹) coexists with CH₄ on the catalyst surface. When the inlet gas is switched to 10% H₂/N₂, the band intensities of HCOO* and *CHO gradually weaken and finally disappear, accompanied by the appearance of CH₄, indicating that CH₄ was produced by the further hydrogenation of *CHO, which was generated by hydrogenation and dehydration of HCOO*. Furthermore, the band of linear-CO* disappears immediately after switching the inlet gas to 10% H₂/N₂, followed by the appearance of CH₄, suggesting that CH₄ was also produced by the hydrogenation of linear-CO* [41]. On the contrary, the band intensity of monodentate carbonate shows no significant change, confirming it is a spectator in this reaction.

For CeO₂/Ni (Fig. 7e), the band (1730 cm⁻¹) of *CHO and two bands (1340 and 1562 cm⁻¹) of HCOO* absorbed on the CeO₂-Ni interface [69] (also can be seen in DFT calculations in Section 3.4) are observed and then disappear along with the appearance of CH₄ band (3017 cm⁻¹), which indicates that a typical formate pathway occurs on CeO₂/Ni for

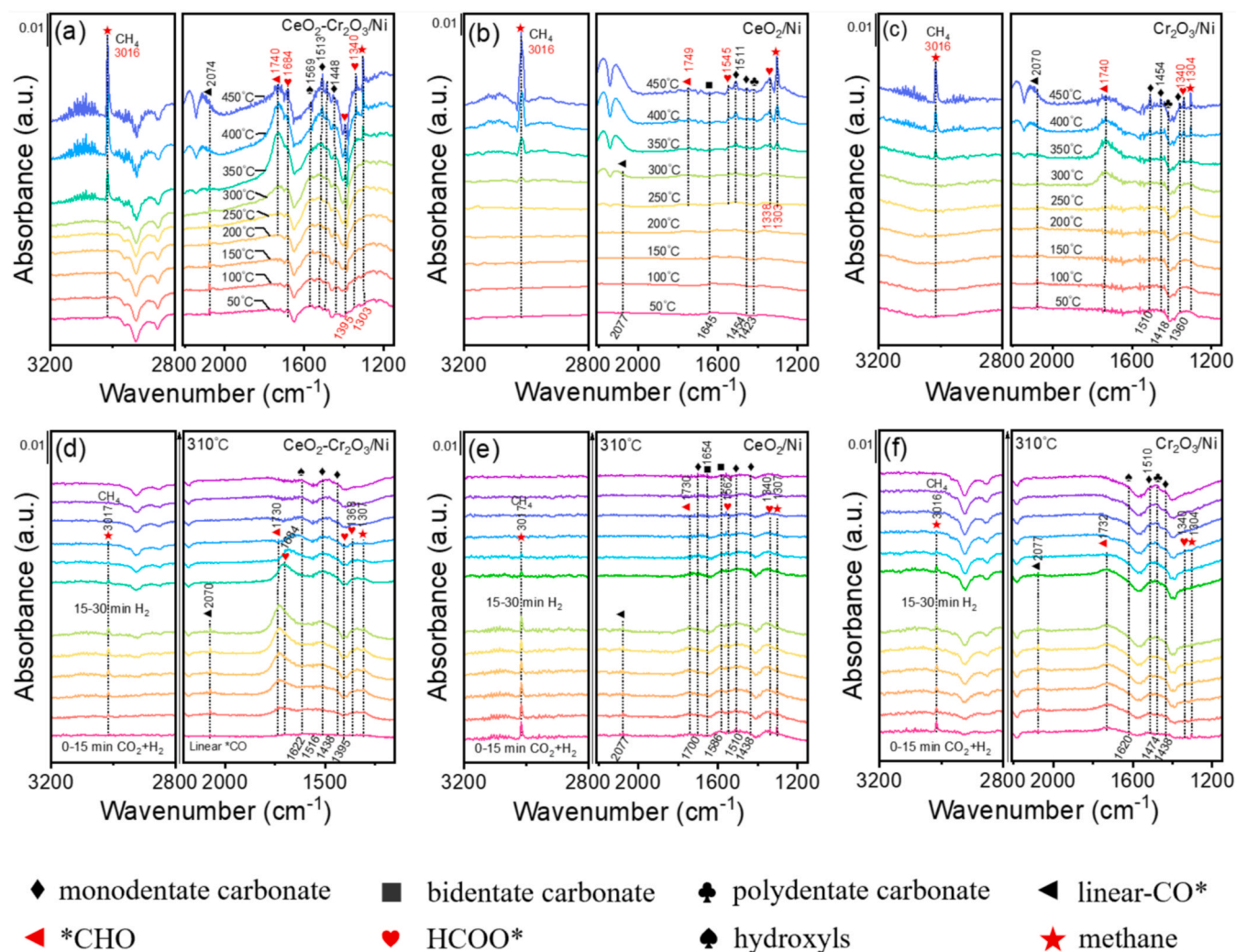


Fig. 7. DRIFTS spectra recorded at different temperatures in 72% H₂/18% CO₂/10% N₂ on (a) CeO₂-Cr₂O₃/Ni, (b) CeO₂/Ni, and (c) Cr₂O₃/Ni; DRIFTS spectra recorded at 310 °C in 72% H₂/18% CO₂/10% N₂ (0–15 min) and then in 10% H₂/N₂ (15–30 min) by switching the inlet gas on (d) CeO₂-Cr₂O₃/Ni, (e) CeO₂/Ni, and (f) Cr₂O₃/Ni.

CO₂ methanation. Besides, a similar trend is also observed for linear-CO*, but its initial peak intensity is very weak. It means that the formate pathway is dominant on CeO₂/Ni rather than the CO pathway, in line with the previous reports [70–73].

For Cr₂O₃/Ni (Fig. 7f), the evolution of carbon species on it is very similar to that on CeO₂-Cr₂O₃/Ni, except that a new band of polydentate carbonate (1474 cm⁻¹) is observed, and the bands of *CHO and HCOO* are obviously weak in intensity. The immediate disappearance of linear-CO* (2077 cm⁻¹) adsorbed on the Cr₂O₃-Ni interface [66] (as revealed in DFT calculations in Section 3.4) after switching the inlet gas illustrates that CH₄ is produced mainly through the CO pathway on Cr₂O₃/Ni. On all three catalysts, after switching the inlet gas to 10% H₂/N₂, we undoubtedly observed a change in the intensity of CHO* -species, indicating it will be formed by further hydrogenation of HCOO* and CO* intermediates. Based on these results, we can deduce that the formate pathway prevails over the CeO₂/Ni catalyst with CeO₂-Ni interfaces, while the CO pathway mainly occurs over the Cr₂O₃/Ni catalyst with the Cr₂O₃-Ni interfaces. For CeO₂-Cr₂O₃/Ni, CO₂ methanation follows both the formate and CO pathways, in which CO₂ is more easily activated and further hydrogenated, explaining its excellent performance in CO₂ methanation. The DFT calculations can further prove these conclusions.

3.4. DFT calculations

To verify the role of CeO₂-Ni and Cr₂O₃-Ni interfaces in CO₂ activation, we calculated the adsorption energy of CO₂ on the two interfaces (Fig. 8). Ni particle, CeO₂ cluster, and Cr₂O₃ cluster models are used to simulate the adsorption behavior of the oxide/Ni inverse catalysts (Fig. S3). As shown in Fig. 8a and b, the CO₂ adsorption energy is -0.10 eV on the CeO₂-Ni interface and -0.41 eV on the Cr₂O₃-Ni interface, indicating that CO₂ molecules prefer to adsorb on the interface with the presence of Cr. Based on the adsorption calculation results, the energy profiles of different reaction routes are calculated (Fig. 8c-f). On the one hand, when the CO₂ molecules adsorb on the CeO₂-Ni and Cr₂O₃-Ni interfaces, the energy barrier to be overcome to generate the HCOO* intermediate is 1.66 and 2.04 eV, respectively, indicating that CO₂ hydrogenation to HCOO* on the CeO₂-Ni interface is easier. On the other hand, the energy barrier for dissociating CO₂ into CO* on the CeO₂-Ni and Cr₂O₃-Ni interfaces is 1.97 eV and 1.40 eV, respectively, indicating that the Cr₂O₃-Ni interface provides a more suitable environment for CO₂ dissociation. It is worth noting that the energy barrier to be overcome for CO₂ dissociation on Cr₂O₃-Ni is lower than that for CO₂ hydrogenation to generate HCOO* on the CeO₂-Ni interface; thus, CO₂ is more favorable to dissociate into CO* on CeO₂-Cr₂O₃/Ni with these two kinds of interfaces, which is in agreement with the in situ DRIFTS results (Fig. 7). For better comparisons, the CO₂ adsorptions and

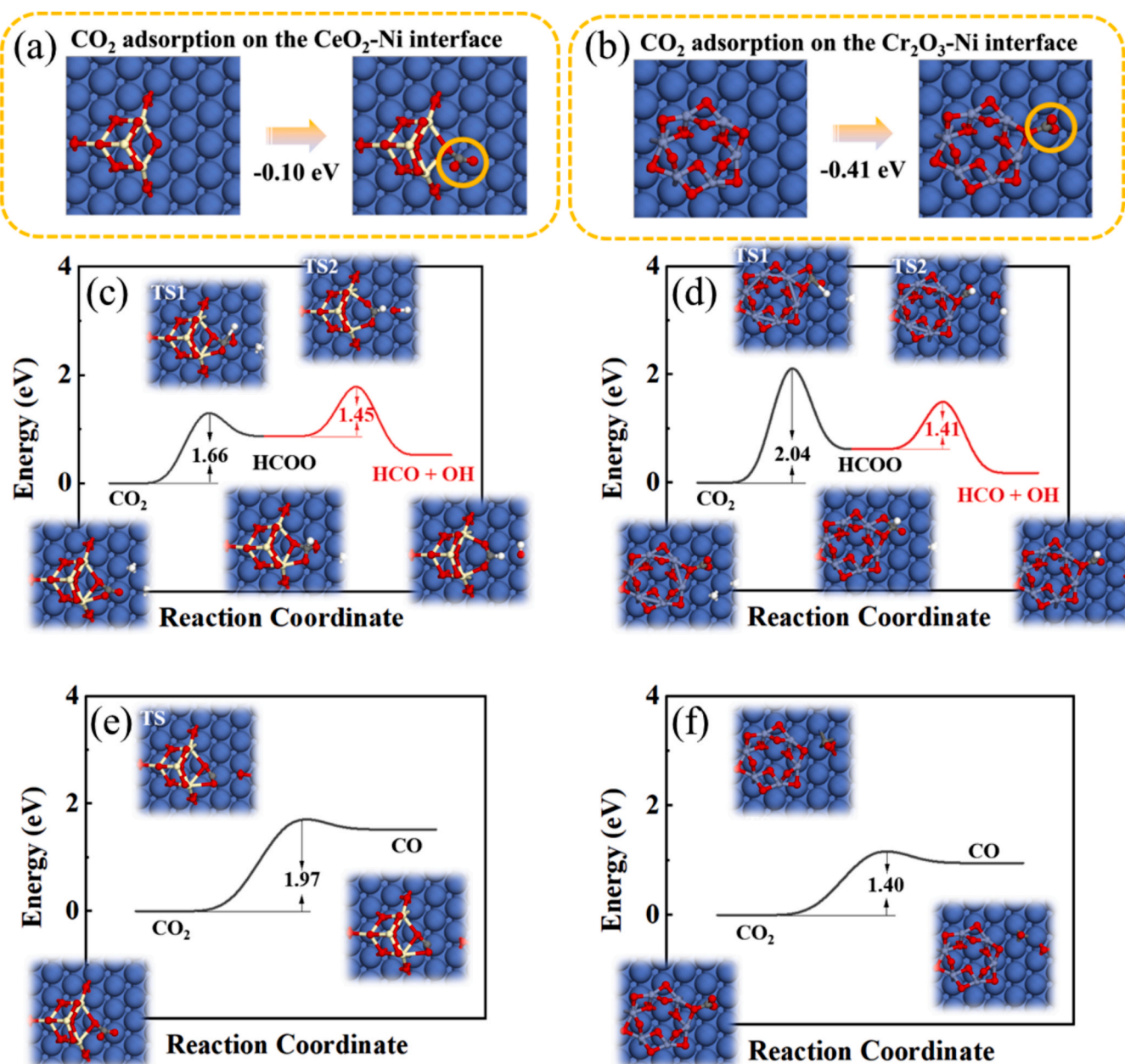


Fig. 8. The adsorption of CO₂ on the different interfaces: CO₂ adsorbs on the CeO₂-Ni interface (a) and on the Cr₂O₃-Ni interface (b); the calculated energy profiles of different reaction routes. CO₂* + H* → HCOO* on the CeO₂-Ni interface (c) and on the Cr₂O₃-Ni interface (d), CO₂* → CO* + O* on the CeO₂-Ni interface (e) and on the Cr₂O₃-Ni interface (f).

the H₂ dissociations over the CeO₂-Cr₂O₃ surface and CeO₂-Cr₂O₃-Ni surface are also calculated, and the results are shown in Figs. S6-S9.

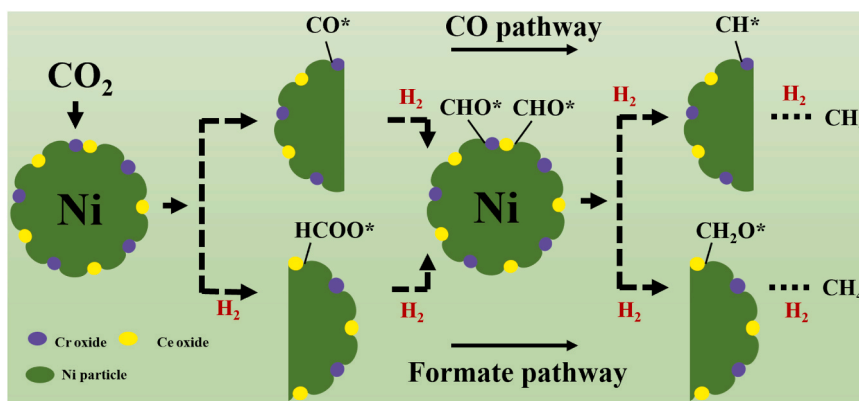
3.5. Proposed catalytic mechanism on CeO₂-Cr₂O₃/Ni

From the in situ DRIFTS and theoretical calculation results, it can be suggested that the tendency of the reaction mechanism occurring on the Cr₂O₃-Ni interface and the CeO₂-Ni interface is different (Scheme 2). On the former, CO₂ is first dissociated to CO* and then hydrogenated to CHO*, which is ultimately hydrogenated to generate CH₄; on the latter, CO₂ is first hydrogenated to HCOO* and then decomposed to CHO* and finally hydrogenated to CH₄. CeO₂-Cr₂O₃/Ni exhibits both the CeO₂-Ni and Cr₂O₃-Ni interfaces. Thus, CO₂ methanation over CeO₂-Cr₂O₃/Ni proceeds via both the CO and the formate pathways. Since the energy barrier to be overcome for CO₂ dissociation on the Cr₂O₃-Ni interface is lower than that for CO₂ hydrogenation to generate HCOO* on the CeO₂-

Ni interface, the introduction of Cr species into the CeO₂-Ni system promotes the activation of CO₂, thus contributing to the high CO₂ conversion of CeO₂-Cr₂O₃/Ni.

4. Conclusions

The roles of CeO₂-Ni and Cr₂O₃-Ni interfaces on CO₂ activation and reaction pathway in CO₂ methanation have been investigated over the inverse CeO₂-Cr₂O₃/Ni model catalysts synthesized by the ion-exchange method. Experimental and DFT calculation results show that the presence of Cr oxides alters the interfaces between Ni and the nearby Ce oxides through electron transfer, forming the special CeO₂-Ni and Cr₂O₃-Ni interfaces to promote CO₂ activation. The formate and CO pathways coexist on CeO₂-Cr₂O₃/Ni, while the formate pathway dominates on the CeO₂-Ni interface, and the CO pathway dominates on the Cr₂O₃-Ni interface. Thus, compared to the catalysts with a single type of



Scheme 2. Schematic diagram of the reaction mechanisms for CO₂ methanation over CeO₂-Cr₂O₃/Ni.

interface, both interfaces in CeO₂-Cr₂O₃/Ni function cooperatively to promote CH₄ production, in which the Cr₂O₃-Ni interface exhibits a relatively lower CO₂ absorption energy and activation energy barrier for CO₂ dissociation to CO, favorable for CO₂ activation and further hydrogenation. Thus, the electron transfer of the special oxide-metal interfaces on CO₂ adsorption and activation is clarified in this work.

CRediT authorship contribution statement

Junbo Tian: Methodology, Validation, Formal analysis, Investigation, Data curation, Writing – original draft, Visualization. **Peng Zheng:** Methodology, Software, Data curation. **Tengfei Zhang:** Visualization. **Zhennan Han:** Conceptualization, Methodology, Writing – review & editing. **Wenqing Xu:** Methodology, Writing – review & editing, Visualization, Funding acquisition. **Fangna Gu:** Methodology, Writing – review & editing, Visualization, Funding acquisition. **Fang Wang:** Writing – review & editing, Funding acquisition. **Zhanguo Zhang:** Writing – review & editing. **Ziyi Zhong:** Writing – review & editing, Funding acquisition. **Fabing Su:** Writing – review & editing, Visualization, Supervision, Funding acquisition. **Guangwen Xu:** Writing – review & editing, Visualization, Supervision.

Declaration of Competing Interest

The authors declare that they have no known competing financial interests or personal relationships that could have appeared to influence the work reported in this paper.

Data availability

Data will be made available on request.

Acknowledgement

This research was funded by the National Key R&D Program of China (No. 2022YFE0208100), National Natural Science Foundation of China (22278405, 22278006, and 52222005), and the Open Project Fund from Guangdong Provincial Key Laboratory of Materials and Technology for Energy Conversion, Guangdong Technion-Israel Institute of Technology (No. MATEC2022KF004).

Appendix A. Supporting information

Supplementary data associated with this article can be found in the online version at [doi:10.1016/j.apcatb.2023.123121](https://doi.org/10.1016/j.apcatb.2023.123121).

References

- [1] Y. Li, Y. Zhang, K. Qian, W. Huang, Metal-support interactions in metal/oxide catalysts and oxide-metal interactions in oxide/metal inverse catalysts, *ACS Catal.* 12 (2022) 1268–1287.
- [2] A.R. Puigdollers, P. Schlexer, S. Tosoni, G. Pacchioni, Increasing oxide reducibility: The role of metal/oxide interfaces in the formation of oxygen vacancies, *ACS Catal.* 7 (2017) 6493–6513.
- [3] J. Zecevic, G. Vanbutsele, K.P. de Jong, J.A. Martens, Nanoscale intimacy in bifunctional catalysts for selective conversion of hydrocarbons, *Nature* 528 (2015) 245–248.
- [4] P.M. Arnal, M. Comotti, F. Schuth, High-temperature-stable catalysts by hollow sphere encapsulation, *Angew. Chem. Int. Ed.* 45 (2006) 8224–8227.
- [5] S.J. Tauster, Strong metal-support interactions, *Acc. Chem. Res.* 20 (1987) 389–394.
- [6] Y. Zhang, X. Yang, X. Yang, H. Duan, H. Qi, Y. Su, B. Liang, H. Tao, B. Liu, D. Chen, X. Su, Y. Huang, T. Zhang, Tuning reactivity of Fischer-Tropsch synthesis by regulating TiO_x overlayer over Ru/TiO₂ nanocatalysts, *Nat. Commun.* 11 (2020) 3185.
- [7] Y. Zhang, J.-X. Liu, K. Qian, A. Jia, D. Li, L. Shi, J. Hu, J. Zhu, W. Huang, Structure sensitivity of Au-TiO₂ strong metal-support interactions, *Angew. Chem. Int. Ed.* 60 (2021) 12074–12081.
- [8] T. Fujita, P. Guan, K. McKenna, X. Lang, A. Hirata, L. Zhang, T. Tokunaga, S. Arai, Y. Yamamoto, N. Tanaka, Y. Ishikawa, N. Asao, Y. Yamamoto, J. Erlebacher, M. Chen, Atomic origins of the high catalytic activity of nanoporous gold, *Nat. Mater.* 11 (2012) 775–780.
- [9] T. Pu, W. Zhang, M. Zhu, Engineering heterogeneous catalysis with strong metal-support interactions: characterization, theory and manipulation, *Angew. Chem. Int. Ed.* 62 (2022), e202212278.
- [10] C. Zhang, L. Wang, U.J. Etim, Y. Song, O.M. Gazit, Z. Zhong, Oxygen vacancies in Cu/TiO₂ boost strong metal-support interaction and CO₂ hydrogenation to methanol, *J. Catal.* 413 (2022) 284–296.
- [11] R.N. d'Aloncourt, M. Friedrich, E. Kunkes, D. Rosenthal, F. Girgsdies, B. Zhang, L. Shao, M. Schuster, M. Behrens, R. Schloegl, Strong metal-support interactions between palladium and iron oxide and their effect on CO oxidation, *J. Catal.* 317 (2014) 220–228.
- [12] Z. Chen, L. Liang, H. Yuan, H. Liu, P. Wu, M. Fu, J. Wu, P. Chen, Y. Qiu, D. Ye, L. Chen, Reciprocal regulation between support defects and strong metal-support interactions for highly efficient reverse water gas shift reaction over Pt/TiO₂ nanosheets catalysts, *Appl. Catal., B* 298 (2021), 120507.
- [13] L. Deng, H. Miura, T. Shishido, S. Hosokawa, K. Teramura, T. Tanaka, Strong metal-support interaction between Pt and SiO₂ following high-temperature reduction: a catalytic interface for propane dehydrogenation, *Chem. Commun.* 53 (2017) 6937–6940.
- [14] X. Xu, T. Lan, G. Zhao, Q. Nie, F. Jiang, Y. Lu, Interface-hydroxyl enabling methanol steam reforming toward CO-free hydrogen production over inverse ZrO₂/Cu catalyst, *Appl. Catal., B* 334 (2023), 122839.
- [15] G.-S. Wu, D.-S. Mao, G.-Z. Lu, Y. Cao, K.-N. Fan, The role of the promoters in Cu based catalysts for methanol steam reforming, *Catal. Lett.* 130 (2009) 177–184.
- [16] T. Shodiya, O. Schmidt, W. Peng, N. Hotz, Novel nano-scale Au/alpha-Fe₂O₃ catalyst for the preferential oxidation of CO in biofuel reformat gas, *J. Catal.* 300 (2013) 63–69.
- [17] C. Wu, L. Lin, J. Liu, J. Zhang, F. Zhang, T. Zhou, N. Rui, S. Yao, Y. Deng, F. Yang, W. Xu, J. Luo, Y. Zhao, B. Yan, X. Wen, J.A. Rodriguez, D. Ma, Inverse ZrO₂/Cu as a highly efficient methanol synthesis catalyst from CO₂ hydrogenation, *Nat. Commun.* 11 (2020) 5767.
- [18] G.-M. Schwab, Electronics of supported catalysts, *Adv. Catal.* 27 (1979) 1–22.
- [19] K. Qian, H. Duan, Y. Li, W. Huang, Electronic oxide-metal strong interaction (EOMS), *Chem. Eur. J.* 26 (2020) 13538–13542.
- [20] J.A. Rodriguez, J. Hrbek, Inverse oxide/metal catalysts: A versatile approach for activity tests and mechanistic studies, *Surf. Sci.* 604 (2010) 241–244.
- [21] J.A. Rodriguez, P. Liu, J. Graciani, S.D. Senanayake, D.C. Grinter, D. Stacchiola, J. Hrbek, J. Fernandez-Sanz, Inverse oxide/metal catalysts in fundamental studies

- and practical applications: A perspective of recent developments, *J. Phys. Chem. Lett.* 7 (2016) 2627–2639.
- [22] R.M. Palomino, R.A. Gutierrez, Z. Liu, S. Tenney, D.C. Grinter, E. Crumlin, I. Walyuo, P.J. Ramirez, J.A. Rodriguez, S.D. Senanayake, Inverse catalysts for CO oxidation: enhanced oxide-metal interactions in MgO/Au(111), CeO₂/Au(111), and TiO₂/Au(111), *ACS Sustain. Chem. Eng.* 5 (2017) 10783–10791.
- [23] M. Mahapatra, R.A. Gutierrez, J. Kang, N. Rui, R. Hamlyn, Z. Liu, I. Orozco, P. J. Ramirez, S.D. Senanayake, J.A. Rodriguez, The behavior of inverse oxide/metal catalysts: CO oxidation and water-gas shift reactions over ZnO/Cu(111) surfaces, *Surf. Sci.* 681 (2019) 116–121.
- [24] Y. Zhu, X. Zhang, K. Koh, L. Kovarik, J.L. Fulton, K.M. Rosso, O.Y. Gutierrez, Inverse iron oxide/metal catalysts from galvanic replacement, *Nat. Commun.* 11 (2020) 3269.
- [25] J. Kang, N. Rui, E. Huang, Y. Tian, M. Mahapatra, R. Rosales, I. Orozco, R. Shi, S. D. Senanayake, P. Liu, J.A. Rodriguez, Surface characterization and methane activation on SnO₂/Cu₂O/Cu(111) inverse oxide/metal catalysts, *Phys. Chem. Chem. Phys.* 23 (2021) 17186–17196.
- [26] M.A.A. Aziz, A.A. Jalil, S. Triwahyono, A. Ahmad, CO₂ methanation over heterogeneous catalysts: recent progress and future prospects, *Green. Chem.* 17 (2015) 2647–2663.
- [27] X. Jia, X. Zhang, N. Rui, X. Hu, C. Liu, Structural effect of Ni/ZrO₂ catalyst on CO₂ methanation with enhanced activity, *Appl. Catal., B* 244 (2019) 159–169.
- [28] R.-P. Ye, Q. Li, W. Gong, T. Wang, J.J. Razink, L. Lin, Y.-Y. Qin, Z. Zhou, H. Adidharma, J. Tang, A.G. Russell, M. Fan, Y.-G. Yao, High-performance of nanostructured Ni/CeO₂ catalyst on CO₂ methanation, *Appl. Catal., B* 268 (2020), 118474.
- [29] A. Cardenas-Arenas, A. Quindimil, A. Davo-Quinonero, E. Bailon-Garcia, D. Lozano-Castello, U. De-La-Torre, B. Pereda-Ayo, J.A. Gonzalez-Marcos, J. R. Gonzalez-Velasco, A. Bueno-Lopez, Isotopic and in situ DRIFTS study of the CO₂ methanation mechanism using Ni/CeO₂ and Ni/Al₂O₃ catalysts, *Appl. Catal., B* 265 (2020), 118538.
- [30] M. Li, H. Amari, A.C. van Veen, Metal-oxide interaction enhanced CO₂ activation in methanation over ceria supported nickel nanocrystallites, *Appl. Catal., B* 239 (2018) 27–35.
- [31] J. Li, Y. Lin, X. Pan, D. Miao, D. Ding, Y. Cui, J. Dong, X. Bao, Enhanced CO₂ methanation activity of Ni/anatase catalyst by tuning strong metal-support interactions, *ACS Catal.* 9 (2019) 6342–6348.
- [32] C. Song, Q. Zhan, F. Liu, C. Wang, H. Li, X. Wang, X. Guo, Y. Cheng, W. Sun, L. Wang, J. Qian, B. Pan, Overturned loading of inert CeO₂ to active Co₃O₄ for unusually improved catalytic activity in fenton-like reactions, *Angew. Chem. Int. Ed.* 61 (2022), 202200406.
- [33] T. Zhang, Q. Liu, Lanthanum-modified MCF-derived nickel phyllosilicate catalyst for enhanced CO₂ methanation: A comprehensive study, *ACS Appl. Mater. Interfaces* 12 (2020) 19587–19600.
- [34] G. Kresse, J. Furthmuller, Efficient iterative schemes for ab initio total-energy calculations using a plane-wave basis set, *Phys. Rev. B* 54 (1996) 11169–11186.
- [35] G. Kresse, J. Furthmuller, Efficiency of Ab-Initio total energy calculations for metals and semiconductors using a plane-wave basis set, *Comput. Mater. Sci.* 6 (1996) 15–50.
- [36] J. Perdew, K. Burke, M. Ernzerhof, Generalized gradient approximation made simple, *Phys. Rev. Lett.* 77 (1996) 3865–3868.
- [37] S. Dudarev, G. Botton, S. Savrasov, C. Humphreys, A. Sutton, Electron-energy-loss spectra and the structural stability of nickel oxide: An LSDA+U study, *Phys. Rev. B* 57 (1998) 1505–1509.
- [38] G. Henkelman, H. Jonsson, Improved tangent estimate in the nudged elastic band method for finding minimum energy paths and saddle points, *J. Chem. Phys.* 113 (2000) 9978–9985.
- [39] H. Fu, J. Liu, N.M. Bedford, Y. Wang, J. Sun, Y. Zou, M. Dong, J. Wright, H. Diao, P. Liu, H. Yang, H. Zhao, Synergistic Cr₂O₃@Ag heterostructure enhanced electrocatalytic CO₂ reduction to CO, *Adv. Mater.* 34 (2022), 2202854.
- [40] P. Hongmanorom, J. Ashok, P. Chirawatkul, S. Kawi, Interfacial synergistic catalysis over Ni nanoparticles encapsulated in mesoporous ceria for CO₂ methanation, *Appl. Catal., B* 297 (2021), 120454.
- [41] X. Xu, L. Liu, Y. Tong, X. Fang, J. Xu, D.-E. Jiang, X. Wang, Facile Cr³⁺-doping strategy dramatically promoting Ru/CeO₂ for low-temperature CO₂ methanation: unraveling the roles of surface oxygen vacancies and hydroxyl groups, *ACS Catal.* 11 (2021) 5762–5775.
- [42] C. Khajonvittayakul, V. Tongnan, S. Amornraksa, N. Laosiripojana, M. Hartley, U. W. Hartley, CO₂ hydrogenation to synthetic natural gas over Ni, Fe and Co-based CeO₂-Cr₂O₃, *Catalysts* 11 (2021) 1159.
- [43] Z. Zhu, K. Feng, C. Li, R. Tang, M. Xiao, R. Song, D. Yang, B. Yan, L. He, Stabilization of exposed metal nanocrystals in high-temperature heterogeneous catalysis, *Adv. Mater.* 34 (2022), 2108727.
- [44] H. Muroyama, Y. Tsuda, T. Asakoshi, H. Masitah, T. Okanishi, T. Matsui, K. Eguchi, Carbon dioxide methanation over Ni catalysts supported on various metal oxides, *J. Catal.* 343 (2016) 178–184.
- [45] S. Lee, Y. Lee, D. Moon, J.Y. Ahn, D.D. Nguyen, S. Chang, S. Kim, Reaction mechanism and catalytic impact of Ni/CeO_{2-x} catalyst for low-temperature CO₂ methanation, *Ind. Eng. Chem. Res.* 58 (2019) 8656–8662.
- [46] K. Jiang, Y. Men, S. Liu, J. Wang, W. An, H. Yu, E.W. Shin, Highly stable and selective Co₂Ni₃TiO₃ for CO₂ methanation: Electron transfer and interface interaction, *J. CO₂ Util.* 53 (2021), 101743.
- [47] Y. Li, Y. Men, S. Liu, J. Wang, K. Wang, Y. Tang, W. An, X. Pan, L. Li, Remarkably efficient and stable Ni/Y₂O₃ catalysts for CO₂ methanation: Effect of citric acid addition, *Appl. Catal., B* 293 (2021), 120206.
- [48] W. Li, X. Nie, X. Jiang, A. Zhang, F. Ding, M. Liu, Z. Liu, X. Guo, C. Song, ZrO₂ support imparts superior activity and stability of Co catalysts for CO₂ methanation, *Appl. Catal., B* 220 (2018) 397–408.
- [49] S. Sun, H. Sun, S. Guan, S. Xu, C. Wu, Integrated CO₂ capture and methanation on Ru/CeO₂-MgO combined materials: Morphology effect from CeO₂ support, *Fuel* 317 (2022), 123420.
- [50] W. Wang, W. Geng, L. Zhang, Z. Zhao, Z. Zhang, T. Ma, C. Cheng, X. Liu, Y. Zhang, S. Li, Molybdenum oxycarbide supported Rh-clusters with modulated interstitial C-O microenvironments for promoting hydrogen evolution, *Small* (2022), 2206808.
- [51] Z. Li, Y. Liu, A. Zhang, Q. Liu, C. Shen, F. Wu, C. Xu, M. Chen, H. Fu, C. Zhou, Quasi-two-dimensional -Ga₂O₃ field effect transistors with large drain current density and low contact resistance via controlled formation of interfacial oxygen vacancies, *Nano Res* 12 (2019) 143–148.
- [52] X. Liu, K. Zhou, L. Wang, B. Wang, Y. Li, Oxygen vacancy clusters promoting reducibility and activity of ceria nanorods, *J. Am. Chem. Soc.* 131 (2009) 3140–3141.
- [53] Y. Zhang, J. Lu, L. Zhang, T. Fu, J. Zhang, X. Zhu, X. Gao, D. He, Y. Luo, D. D. Dionysiou, W. Zhu, Investigation into the catalytic roles of oxygen vacancies during gaseous styrene degradation process via CeO₂ catalysts with four different morphologies, *Appl. Catal., B* 309 (2022), 121249.
- [54] Z. Zhang, J.T. Yates, Band bending in semiconductors: chemical and physical consequences at surfaces and interfaces, *Chem. Rev.* 112 (2012) 5520–5551.
- [55] J. Ohyama, A. Yamamoto, K. Teramura, T. Shishido, T. Tanaka, Modification of metal nanoparticles with TiO₂ and metal-support interaction in photodeposition, *ACS Catal.* 1 (2011) 187–192.
- [56] T. Zhang, W. Wang, F. Gu, W. Xu, J. Zhang, Z. Li, T. Zhu, G. Xu, Z. Zhong, F. Su, Enhancing the low-temperature CO₂ methanation over Ni/La-CeO₂ catalyst: The effects of surface oxygen vacancy and basic site on the catalytic performance, *Appl. Catal., B* 312 (2022), 121385.
- [57] Z. Mao, P.G. Lustemberg, J.R. Rumpitz, M. Veronica Ganduglia-Pirovano, C. T. Campbell, Ni nanoparticles on CeO₂(111): energetics, electron transfer, and structure by Ni adsorption calorimetry, spectroscopies, and density functional theory, *ACS Catal.* 10 (2020) 5101–5114.
- [58] Y. Yin, J. Yin, W. Zhang, H. Tian, Z. Hu, M. Ruan, H. Xu, L. Liu, X. Yan, D. Chen, FT-IR and micro-Raman spectroscopic characterization of minerals in high-calcium coal ashes, *J. Energy Inst.* 91 (2018) 389–396.
- [59] S. Dutta, A. Pandey, Leeladhar, K.K. Jain, Growth and characterization of ultrathin TiO₂-Cr₂O₃ nanocomposite films, *J. Alloy. Compd.* 696 (2017) 376–381.
- [60] R. Long, Y. Huang, H. Wan, Surface oxygen species over cerium oxide and their reactivities with methane and ethane by means of in situ confocal microprobe raman spectroscopy, *J. Raman Spectrosc.* 28 (1997) 29–32.
- [61] H. Yang, G. Dai, Z. Chen, J. Wu, H. Huang, Y. Liu, M. Shao, Z. Kang, Pseudo-periodically coupling Ni-O lattice with Ce-O lattice in ultrathin heteronanowire arrays for efficient water oxidation, *Small* 17 (2021), 2101727.
- [62] L. He, B.L. Liang, L. Li, X.F. Yang, Y.Q. Huang, A.Q. Wang, X.D. Wang, T. Zhang, Cerium-oxide-modified nickel as a non-noble metal catalyst for selective decomposition of hydrous hydrazine to hydrogen, *ACS Catal.* 5 (2015) 1623–1628.
- [63] N. Wang, W. Qian, W. Chu, F. Wei, Crystal-plane effect of nanoscale CeO₂ on the catalytic performance of Ni/CeO₂ catalysts for methane dry reforming, *Catal. Sci. Technol.* 6 (2016) 3594–3605.
- [64] J. Gao, Y. Wang, Y. Ping, D. Hu, G. Xu, F. Gu, F. Su, A thermodynamic analysis of methanation reactions of carbon oxides for the production of synthetic natural gas, *RSC Adv.* 2 (2012) 2358–2368.
- [65] J. Zeng, Y. Sun, J. Zhang, Z. Chang, J. Yang, J. Liu, J. Li, F. Yu, Fabrication of surface oxygen vacancies on NiMnAl-LDO catalyst by high-shear mixer-assisted preparation for low-temperature CO₂ methanation, *Fuel* 309 (2022), 122099.
- [66] T. Pu, J. Chen, W. Tu, J. Xu, Y.-F. Han, I.E. Wachs, M. Zhu, Dependency of CO₂ methanation on the strong metal-support interaction for supported Ni/CeO₂ catalysts, *J. Catal.* 413 (2022) 821–828.
- [67] B. Zhao, P. Liu, S. Li, H. Shi, X. Jia, Q. Wang, F. Yang, Z. Song, C. Guo, J. Hu, Z. Chen, X. Yan, X. Ma, Bimetallic Ni-Co nanoparticles on SiO₂ as robust catalyst for CO methanation: Effect of homogeneity of Ni-Co alloy, *Appl. Catal., B* 278 (2020), 119307.
- [68] F. Wang, S. He, H. Chen, B. Wang, L. Zheng, M. Wei, D.G. Evans, X. Duan, Active site dependent reaction mechanism over Ru/CeO₂ catalyst toward CO₂ methanation, *J. Am. Chem. Soc.* 138 (2016) 6298–6305.
- [69] K. Feng, J. Tian, M. Guo, Y. Wang, S. Wang, Z. Wu, J. Zhang, L. He, B. Yan, Experimentally unveiling the origin of tunable selectivity for CO₂ hydrogenation over Ni-based catalysts, *Appl. Catal., B* 292 (2021), 120191.
- [70] Y. Du, C. Qin, Y. Xu, D. Xu, J. Bai, G. Ma, M. Ding, Ni nanoparticles dispersed on oxygen vacancies-rich CeO₂ nanoplates for enhanced low-temperature CO₂ methanation performance, *Chem. Eng. J.* 418 (2021), 129402.
- [71] Z. Zhang, K. Feng, B. Yan, Enhanced Ni-Ce interactions to enable efficient low-temperature catalytic CO₂ methanation, *Catal. Sci. Technol.* 12 (2022) 4698–4708.
- [72] J. Zhang, Y. Yang, J. Liu, B. Xiong, Mechanistic understanding of CO₂ hydrogenation to methane over Ni/CeO₂ catalyst, *Appl. Surf. Sci.* 558 (2021), 149866.
- [73] Z. Bian, Y.M. Chan, Y. Yu, S. Kawi, Morphology dependence of catalytic properties of Ni/CeO₂ for CO₂ methanation: A kinetic and mechanism study, *Catal. Today* 347 (2020) 31–38.